ORIGINAL ARTICLE

lajss.org© Latin American Journal of Solids and Structures

www.lajss.org

Bearing capacity of ultra-high-performance concrete jacked pipe: full-scale test and theoretical calculation model

Lei He[a], Li Zhou[b], Shanqing Ma[a]*, Wei Wang[b], Yuan Lu[a], Zengli Shi[a]

[a]China Electric Power Research Institute, Beijing 102401, China. Email: helei2006@126.com, 897610753@qq.com, 462488580@qq.com, 1207174798@qq.com
[b]State Grid Hubei Electric Power Co., Ltd. Economic and Technical Research Institute, Wuhan 430074, China. Email: 396242128@qq.com, 1064662404@qq.com

* Corresponding author

https://doi.org/10.1590/1679-7825/e8510

Abstract

Current pipe jacking projects predominantly use C50 concrete pipes, which are prone to cracking and failure under jacking forces during complex construction. This study investigates the mechanical performance and failure mechanisms of C150 ultra-high performance fibre reinforced concrete (UHPFRC) pipes through full-scale trilateral loading test and numerical simulation. Key outcomes include crack load (232 kN/m), damage load (452 kN/m), and maximum displacements (64.3 mm horizontal, 71.6 mm vertical). Radial loading induced four primary cracks along the inner/outer left-right surfaces of the pipe, accompanied by extensive secondary crack networks. Damage progression began with concrete spalling at the top/bottom due to crack propagation, followed by reinforcement yielding and structural collapse. A predictive model for crack load and ultimate bearing capacity was developed, validated by experimental data. ABAQUS finite element simulations demonstrated excellent correlation with experiments, accurately reproducing macroscopic damage patterns. Notably, UHPFRC pipes exhibited 2.55-fold higher radial bearing capacity compared to C50 counterparts. This research establishes UHPFRC as a superior material for pipe jacking applications, offering enhanced structural integrity and reliability.

Keywords

jacked pipe; UHPFRC; full-scale test; mode of failure; calculation model

Graphical Abstract

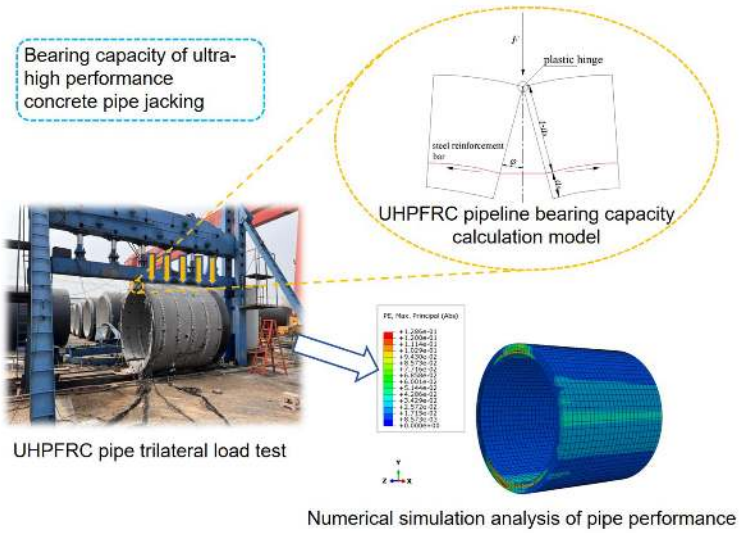

Received december 17, 2024. In revised form february 03, 2025. Accepted march 17, 2025. Available online march 18, 2025.
https://doi.org/10.1590/1679-7825/e8510

Latin American Journal of Solids and Structures. ISSN 1679-7825. Copyright © 2025. This is an Open Access article distributed under the terms of the Creative Commons Attribution License, which permits unrestricted use, distribution, and reproduction in any medium, provided the original work is properly cited.

1 INTRODUCTION

The safety and durability of underground pipelines have become an important issue in urban development with the acceleration of urbanization and the continuous promotion of infrastructure construction. Defects in strength, durability and construction adaptability of ordinary concrete pipelines have become bottlenecks restricting the development of pipe jacking technology.UHPFRC, through its ultra-high mechanical properties, lightweight design and environmentally friendly characteristics, can not only solve the inherent shortcomings of traditional materials, but also promote the development of pipe jacking projects in the direction of long-distance, deep-buried and high-precision. With the large-scale production and cost optimisation of UHPFRC, its application in the field of pipe jacking will accelerate its popularity and become the core direction of the future upgrade of underground engineering materials. [1-5].

Ultra-high-performance fiber-reinforced concrete (UHPFRC), a new type of high-performance concrete material, shows considerable potential for application in structural engineering owing to its mechanical properties, durability, and construction performance., UHPFRC has higher compressive strength, tensile strength and toughness than ordinary concrete, which were achieved by optimizing the particle grading, using ultrafine active mix and efficient additives, and incorporating the toughening effect of microfine steel fibers. UHPFRC has broad application prospects in engineering fields such as bridges, tunnels and pipelines owing to these properties [6-9].

Yan Xinyu et al. [10] studied the mechanical properties of C50 concrete and UHPFRC pipe joints using the flexural and shear strength foot rule tests. The results showed that, when the axial force was unchanged, the larger the eccentricity distance, the smaller the bending stiffness of the pipe joints; the bending stiffness gap tended to decrease with the increase in the axial force of pipe joints of different eccentricity distances for pipe joints with UHPFRC. The bending stiffness and shear strength were of the UHPFRC pipe joints were 1.5-2.0 times higher than those of C50 pipe joints of C50 tube sheet joints.

Liu Libin [11] investigated the crack development in and structural performance of UHPFRC pipe with or without reinforcement with different steel fiber contents. The load carrying capacity and top deflection of the steel-reinforced UHPFRC pipe were 3.2 and 3.5 times higher than those of the unreinforced UHPFRC pipe, respectively; the ultimate load of the reinforced UHPFRC pipe with cracking was 1.32 times higher that of the crack load of the pipe with many and dense cracks.

Yang Yan et al. [12] designed a UHPFRC pipe corridor based on the C40 concrete integrated pipe corridor structure. The results showed that the maintenance time of the precast sections was shortened by 75%, the number of precast section joints per linear meter was reduced by half, the construction period was reduced by 53%, and its whole-life cost was reduced by 37%.

Haktanir et al. [13] investigated the effect of the length of steel fibers on the performance of the pipe, finding that the pipe doped with long steel fiber was stronger.

MacDonald et al. [14] compared the strength, stiffness, and extent of cracks of steel-fiber pipe with that of normal reinforced concrete pipe (RCP). The mechanical properties of the steel-fiber reinforced concrete pipe were substantially better than those of ordinary RCP and of ordinary RCP after cracking.

Park et al. [15] increased the strength and ductility of concrete pipe doped with rubber particles by mixing steel fibers with PP fibers.

Xu Yong [16] determined the contact state according to two situations (without mud and with mud lubrication) in pipe jacking construction. The method of rectangular pipe-soil contact was proposed and the friction model was established. Comparison shows that the model is closer to the field data and verifies its accuracy.

Zhou Yuheng [17] used data from HZMB tunnel, and calculated jacking forces with various formulas and ABAQUS models. Analysis showed JMTA & Shanghai norms overestimated, while Shimada's lower bound approximated measured values. Simulation showed transition from 1/3 to 1/2 soil-pipe contact.

Gong Mingzi et al. [18]studied the impacts of steel fiber embedment depth, diameter, and angle on their pull - out behavior in UHPFRC. Results indicate: deeper embedment raises maximum pull - out force, work, stress, and strength utilization, yet reduces average bond strength; larger diameter increases maximum pull - out force, work, and average bond strength, but decreases strength utilization and maximum pull - out stress; increasing embedment angle makes maximum pull - out force and work peak at 45° and 30° respectively before dropping, with specimens failing by fiber fracture at 75°.

Fiber-reinforced composites have been more widely used in the field of buildings and less in pipeline structures. Therefore, an in-depth study of UHPFRC jacked pipes, their mechanical properties, and their damage modes is required promote the application of UHPFRC in the field of pipeline engineering.

The three-edge bearing test was adopted to analyze the crack development, damage process and load displacement curve of a UHPFRC header pipe during the radial loading process to study its mechanical properties. The aims were to determine the mechanical properties and damage mechanisms of the UHPFRC header pipe and to establish a model for calculating the effects on the UHPFRC header pipe through theoretical research and numerical simulation software. The results of the three-edge bearing test were validated, proving the applicability of the theoretical calculation and numerical simulation model for UHPFRC header pipes.

2 PIPE BEARING PERFORMANCE TEST

2.1 Test pipe size and parameters

Figure 1 shows the actual on-site photograph of the pipe specimen was fabricated for this research. The specifications of the experimental pipe were as follows: an inner diameter of 2.5 meters, a wall thickness of 180 millimeters, and a dual-layer reinforcement configuration with an outer layer of 10 reinforcement elements spaced at 120 millimeters and an inner layer of 10 reinforcement elements spaced at 100 millimeters. The outer and inner protective layers were 30 and 25 millimeters thick, respectively. The pipe was constructed from C150 ultra-high-performance concrete, exhibiting an axial tensile strength of 6.4 MPa, an axial compressive strength of 150 MPa, and a modulus of elasticity of 45.3 GPa. HRB400-grade reinforcement was used, which was characterized by a standard tensile strength of 400 MPa, an ultimate tensile strength of 540 MPa, and a modulus of elasticity of 200 GPa. These material properties were further confirmed using the HRB400-grade specification, which indicated a standard tensile strength of 400 MPa, an ultimate tensile strength of 540 MPa, and a modulus of elasticity of 200 GPa. Figures 2 depict the dimensional and reinforcement schematics.



Figure 1 *Photographs of on-site test pipe processing.*

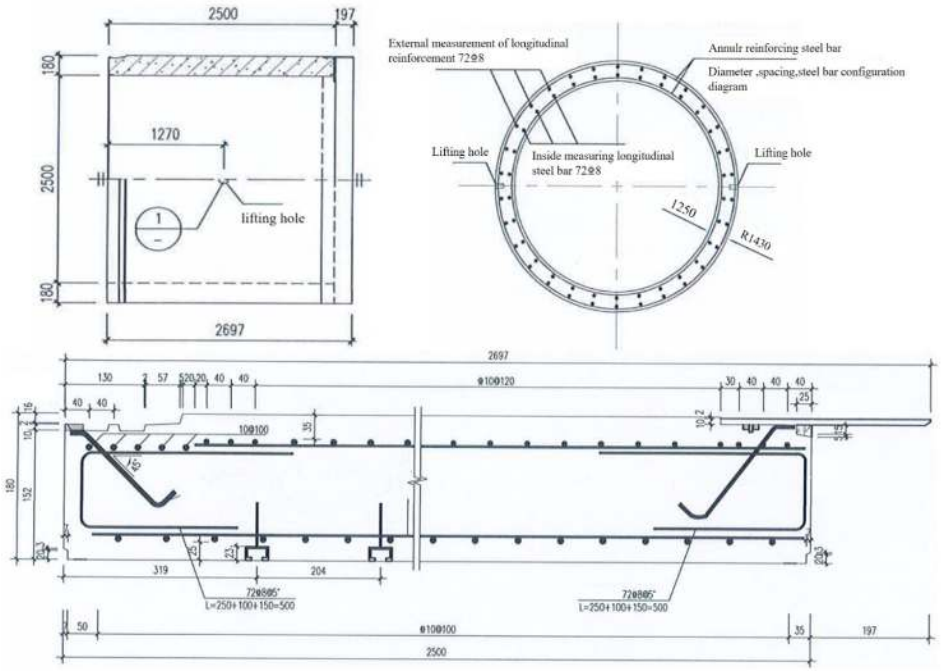

Figure 2 *Test pipe size and reinforcement (unit: mm).*

2.2 Three-edge bearing test

The pipe radial loading test was conducted according to GB/T 16752-2017 “concrete and reinforced concrete drainage pipe test method”. In the three-point test method, the test device consists of a test machine frame, loading equipment, and display instrumentation, as shown in Figure 3..

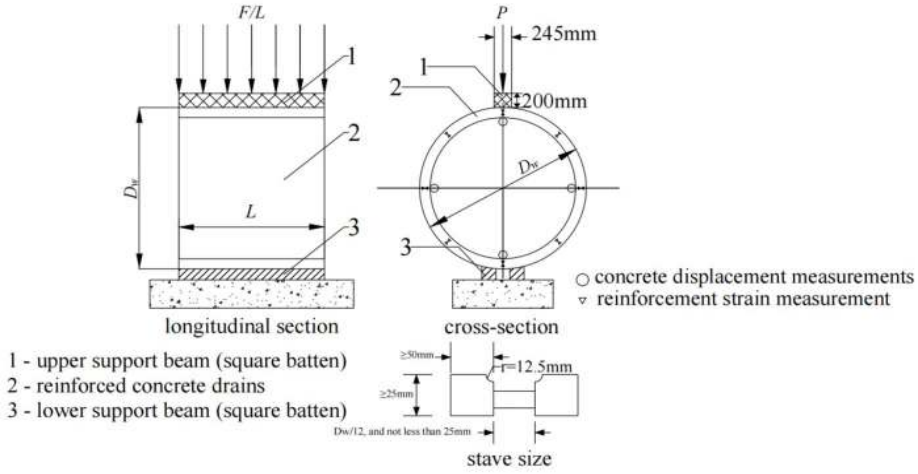

Figure 3 *Three-edge bearing test method, where P is the radial load value; F is the total load value; L is the effective length of the pipe (socketed pipe is the full length of the flat section Lp or the length of the cylindrical unit); Dw is the outer diameter of the pipe.*

In addition to the fixed parts of the test frame, the two supporting beams, upper and lower, could be extended to the entire test length of the test piece. The upper support beam ensured that its bending degree is not more than 1/720 of the length of the test pipe under the maximum load. A rubber mat board was placed between the steel beam and the tube; the length and width of the rubber mat board were the same as those of the steel beam. The rubber mat board was not less than 25 mm thick, and the Shore hardness was 45-60 A. The lower support beam is composed of two hardwoods. Its cross-sectional dimension width is not less than 50 mm, the thickness is not less than 25 mm, and the length is not less than the test length of the pipe. A circular arc with a radius of 12.5 mm should be made at the contact between the lower support beam made of hardwood and the pipe. The net distance between the two lower support beams is 1 / 12 of the outer diameter of the pipe, but it should not be less than 25 mm.

The test radial load was calculated according to Equation (1):

$$P = F/L \tag{1}$$

where P is the radial load, kN/m; F is the total load value, kN; L is the effective length of the pipe (socketed pipe is the full length of the straight section Lp or the length of the cylinder unit), m.



Figure 4 *Three-edge bearing test method device.*

Place the pipe to be tested on the two parallel lower support beams of the external pressure load test device, and then place the upper support beam on the pipe to be tested. In the process of placing, the pipe to be tested and the axes of the upper and lower support beams should be made parallel to each other, and it should be ensured that the upper support beam can move freely in the vertical plane passing through the centre line of the upper and lower support beams. The upper and lower support beams shall cover the effective length of the pipe, and the loading point of the instrument shall be at the midpoint of the full length of the pipe. The test loading system is shown in Figure 4.

2.3 Measurement point arrangement

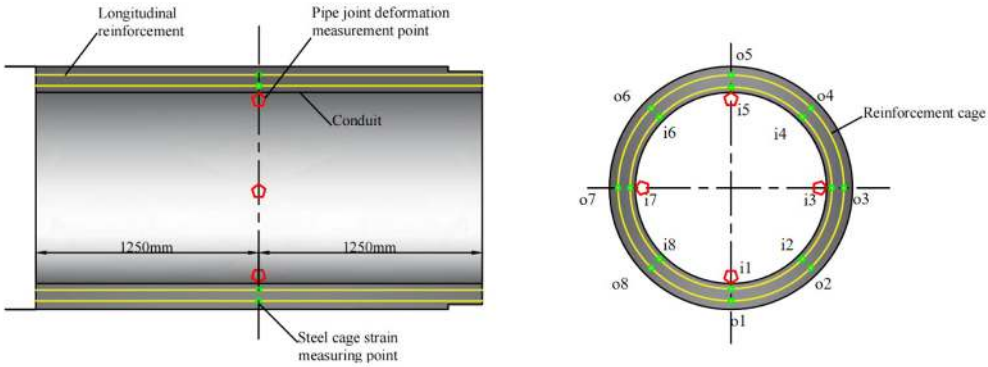

Figure 5 *Pipeline measurement point arrangement.*

The pipeline measurement points were arranged as shown in Figure 5. The monitoring section was located in the radial center of the pipeline, 1250 mm from the mouth of the pipeline, in which the reinforcement strain sensors were arranged in 45° intervals along the inner and outer annular reinforcement ring, for a total of 16 measurement points. The displacement sensors were arranged along the inner wall of the concrete of the monitoring section in 90° intervals, for a total of 4 measurement points.

2.4 Test results and analysis

2.4.1. Pipe Displacement

The load–displacement image of the pipeline is shown in Fig. 6, where Δx and Δy denote the horizonal and vertical displacement during the loading of the pipeline monitoring section, respectively.

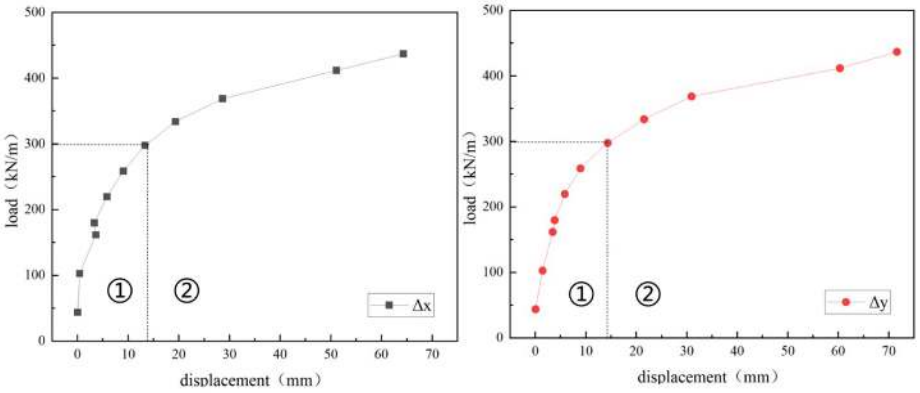

(a) Horizontal load-displacement curve of pipeline *(b) Vertical load-displacement curve of pipeline*

Figure 6 *Horizontal and vertical pipe load–displacement curves.*

Fig. 6 shows that the maximum displacement in the horizontal (Δx) and vertical (Δy) directions of the test pipe were 64.3mm and 71.6mm, respectively. The displacement and deformation of the pipe are divided into two phases: ① During the preloading stage with loads less than 298kN/, the displacement of the pipe in the horizontal and vertical directions increased with increasing load and varied approximately linearly~~-m~~. The whole pipe is in the elastic deformation stage. ② When the load exceeds 298kN/m, the displacement of the pipe in the horizontal and vertical

directions more quickly increases the elastic deformation stage due to cracks appearing in the pipe. The cracks in the pipeline continue to develop in various directions with increasing load, leading to the failure of the structural stability of the pipeline and to the rapid increase in the displacement of the pipeline.

When loaded to 412 kN/m, the horizontal and vertical displacements of the pipeline rapidly increased compared with those under the previous load. The pipeline structure was damaged, the horizontal displacement of the pipeline reached its maximum (64.3 mm), and the vertical displacement was 71.6 mm when loaded to 437 kN/m. The displacement of the pipeline under the cracking load was 9.02% (Δx) versus 8.10% (Δy) of that of the pipeline under the destructive load.

2.4.2. Crack test results

Fig. 7 shows that the top bottom left side and the right side of the pipe were squarely defined at the pipe socket. The bottom outer, left inner, and right inner walls of the pipe were unaffected during radial loading because no cracks appeared in the top outer wall. The following descriptions of the top, bottom, left side, and right side refer to the top inner wall, bottom inner wall, left outer wall, and right outer wall of the pipe, respectively.

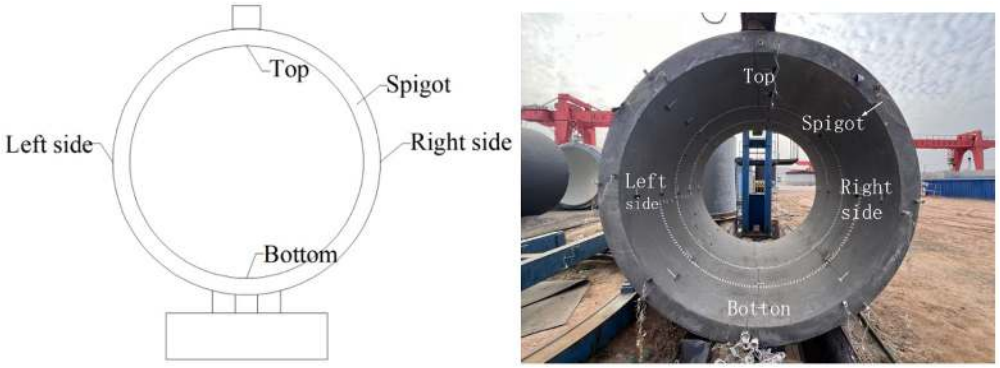

***Figure** 7 Test pipe definitions.*

The crack widths on the top, bottom, left, and right sides of the pipe were monitored during the step-by-step loading process. The maximum crack width was marked when the crack first appeared; thereafter, the crack expansion was monitored in real time at the marking points during the test process. Fig. 8 shows the expansion of the main cracks in the pipe at different loading stages.

Fig. 8 shows that cracks first appeared at the top of the pipe during the loading process, which were followed by cracks on the bottom, left, and right sides. The crack widths at the top, bottom, left, and right of the pipe were 0.2mm, 0.15mm, 0.08mm, and 0.07mm, respectively, when the load was approximately 220kN/m. The development of cracks in all directions was relatively stable when the load was increased from 220kN/m to 298kN/m. A load of 369kN/m led the crack width at the top and bottom of the pipe to rapidly increase, and both exceeded 1mm (Fig. 8). The crack widths on the left and right sides of the pipe were relatively stable with the increase in load, reaching 0.45mm and 0.47mm, respectively. The reinforcement of the tensile zone at the top of the pipe reached the yielding point at a load of 437kN/m, and the crack widths rapidly increased. At this time, the crack widths at the top of the pipe were relatively stable compared with those on the left and right sides of the pipe. The crack width at the top of the pipe was slightly larger than those on the left and right sides of the pipe, at 3.76mm, which was 12.9%, 180.6% and 166.67% larger than the cracks on the bottom (3.33mm), left (1.34mm), and right (1.41mm) of the pipe, respectively.

The crack width was relatively stable with the increase in load during the loading of the initial pipe until the crack load was reached, then into the bending stage of reinforcement. The UHPFRC pipe containing steel fiber in the joint plays a role in the steel reinforcement, having an inhibitory effect on the initial crack development in the pipe, thus increasing the pipe's resistance to cracking.

The distribution and depth of the cracks are shown in Figure 9, where 0°, 90°, 180°, and 270° indicate the top, right side, bottom, and left side of the pipe, respectively. Cracks first appeared on the top of the pipe, followed by cracks on the bottom and left and right sides of the pipe when loaded to 220kN/m, but their distribution was restricted. With increasing load, new cracks developed on the top and bottom of the pipe away from the arching line. New cracks were no longer produced on the top of the pipe when the load exceeded 334kN/m, whereas new cracks were still produced on the bottom of the pipe until the destructive load was reached. The distribution of the cracks on the left and right sides of the pipe increased during the whole loading process. The cracks on the left and right sides of the pipe were distributed close to 90° when the maximum load-bearing capacity of the pipe was reached.

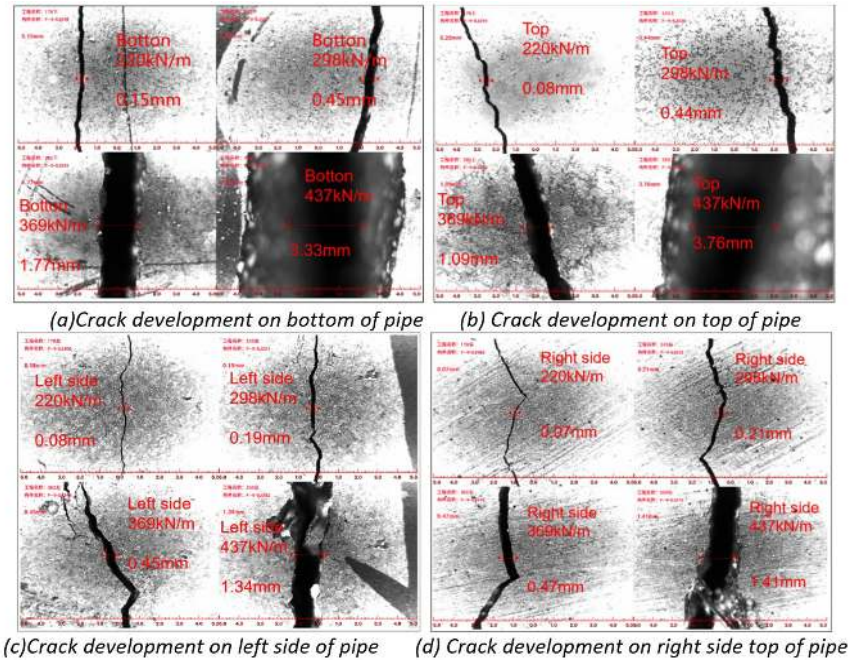

(a)Crack development on bottom of pipe (b) Crack development on top of pipe

(c)Crack development on left side of pipe (d) Crack development on right side top of pipe

Figure 8 *Pipeline cracking development.*

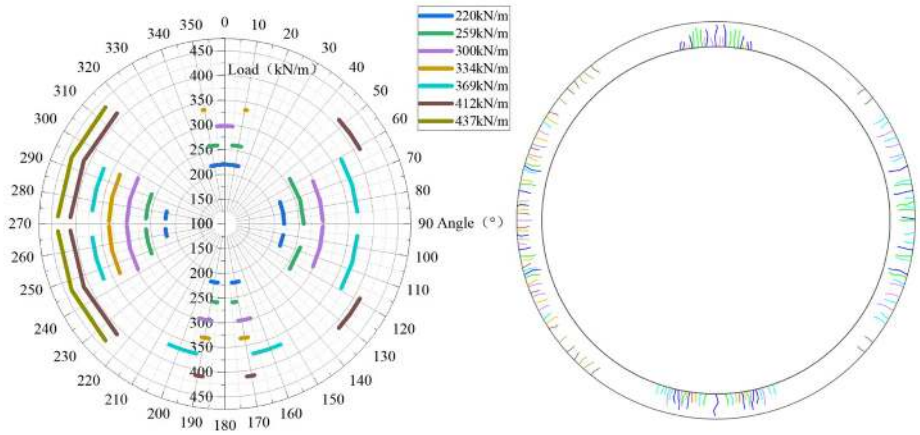

Figure 9 *Distribution of cracks generated under various levels of pipeline loading.*

In summary, under radial loading conditions, the crack pattern at the top and bottom sections of the pipeline were highly concentrated, predominantly manifesting during the early to middle stages of loading. Conversely, the crack distribution across the sides of the pipeline was more extensive, with cracks primarily appearing during the middle to late stages of loading. The progression of cracks in the top and bottom sections was primarily marked by an increase in crack width as the loading intensity increased. Crack progression on the sides was characterized by both an expansion in crack distribution and an elevation in crack count. Furthermore, the sides of the pipeline exhibited a high crack density, with short cracks and a broad distribution. This finding can be attributed to the ability of the steel fibers within the pipeline to redistribute the stresses in the concrete over a larger area, thereby locally mitigating tensile stresses. Notably, the steel fibers demonstrated a substantial capacity to inhibit the widening of the cracks.

2.4.3. Reinforcement strain

Figure 10 shows the load–strain curves of the inner- and outer ring reinforcements of the pipe. The tensile strains were measured at the measuring points used for the reinforcement, except for the compressive strains at points i1, i5, o1, o5, where the compressive strains were collected, because the strain gauges of the inner- and outer ring reinforcements were arranged on the outer side of the circumferential reinforcement under the radial loading condition.

Below 369kN/m, the strains at the measuring points of the inner ring reinforcement gradually increased with the increase in load; the strains at the measuring points on the left side of the pipe, the top of the right side and the bottom

were relatively larger. When loading to 412kN/m, the strain at each measuring point of the inner- and outer ring reinforcements suddenly changed. At a load of 437kN/m, the maximum tensile strain of the pipe ring reinforcement appeared on the right side of the outer ring reinforcement at the o3 measuring point, which was 1863.04με. The yield strain was not yet reached, and the maximum tensile strain appeared at the top of the inner ring reinforcing bar at the i5 measuring point, which was 425.62με. The maximum tensile strain at the top of the inner ring reinforcement at measuring point i5 was -2102.62με; the strain at the top of the pipe inner ring reinforcement was -2102.62με. The maximum tensile strain was -425.62με at point i5 on the top of the inner ring bar; the strain at the top of the inner ring bar of the pipe was -2102.91με; the strain at the bottom of the inner ring bar was -1797.26με, which indicated that the inner ring bar yielded, and the structure of the pipeline was damaged. The ultimate load-bearing capacity of the test pipe was 437kN/m.

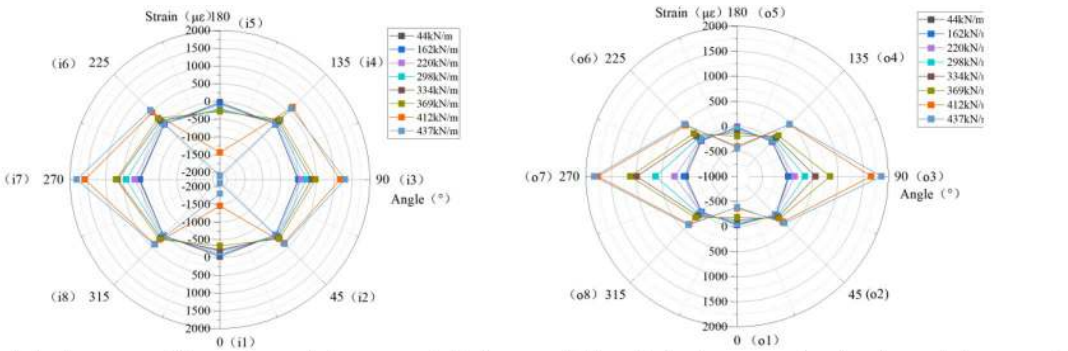

(a) Load-strain curve of inner ring reinforcement of pipe *(b) Load-strain curve of outer ring reinforcement*

Figure 10 *Load–strain curves of steel reinforcement in (a) inner and (b) outer pipe rings.*

2.4.4. Failure mode

Figure 11 illustrates the damage to the test pipes. In the three-side loading test, the stress on the pipe was tensile and compressive on the inside of the top and bottom, respectively; the stress on the left and right sides of the pipe was tensile on the outside and compressive on the inside. Four main cracks appeared on the inside of the top and bottom as well as the left and right outer parts of the pipe. The main cracks deepened and lengthened with increasing load, and numerous secondary cracks were distributed along the periphery of the main cracks. The cracks continued to lengthen until they intersected, and then concrete debris began to fall from within the main cracks. Concrete spalling first appeared in the tensile region. Taking the top of the pipe as an example, the concrete first cracked on the inner side; reinforcement yield deformation occurred with the gradual increase in the load. The concrete starts to separate, and the concrete on the inner wall of the pipe spalled. In this process, the concrete cracked in the tensile zone and gradually separated from the pipe. Ultimately, the reinforcement yielded in the tensile zone, with the cracks extending inward; the concrete compressed in the compression zone but was not crushed.



(a)Bottom of pipe *(b)Top of pipe*

(c)Right side of pipe

Figure 11 *Pipe cracking and damage*

3 CALCULATION MODEL OF UHPFRC PIPELINE BEARING CAPACITY

The results of the three-edge bearing test showed that the main damage type of the pipe under radial loading was yield deformation of the top reinforcement, gradual detachment from of the reinforcement from the concrete, and spalling of the concrete on the inner wall of the pipe. The cross-section at the top of the pipe was crucial. Therefore, the load capacity model of the top of the pipe can be simplified to the theoretical model of the curved beam load capacity for analysis.

3.1 Curved Beam Calculation Model

The curved beam force was simplified to a hingeless arch under concentrated load, and the structure was a cubic superstatic structure, which we solved using the elastic center method. The computational model is shown in Fig. 12.

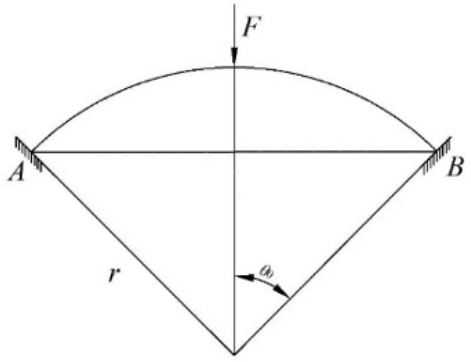

Figure 12 *Curved Beam Calculation Model.*

(1) Selection of foundation system. The symmetrical structure is truncated from the top; the axial force X_1, bending moment X_2, and shear force X_3 at the top are shown in Fig. 13.

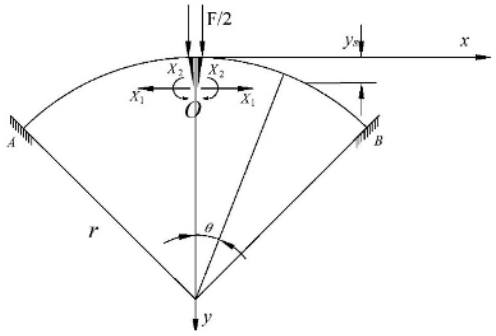

Figure 13 *Base system.*

(2) Determine the position of elastic center O. The coordinates of any point on the arch axis are *x*, *y*; the angle of the center of the circle is ϑ. The distance of point O from the origin of the coordinates, *I.E.*, the length of the rigid arm, y_s, is as follows:

$$y_s = \frac{\int \frac{y}{EI} ds}{\int \frac{1}{EI} ds} = \frac{\int (r - r\cos\theta) r d\theta}{\int r d\theta} = \frac{r(\theta_0 - \sin\theta_0)}{\theta_0} \tag{2}$$

r is the radius of inner wall of a curved beam;

ϑ_0 is the corresponding circumcentric angle of a semicurved beam;

(3) Solve for coefficients δ_{11} and δ_{22}. Only the effect of the bending moments is considered due to the symmetry of the structure, $X_3 = 0$, and the bending moments of the basic structure under the action of $X_1 = 1$ and $X_2 = 1$:

$$\overline{M_1} = y_s - r(1-\cos\theta) = r\left(\cos\theta - \frac{\sin\theta_0}{\theta_0}\right)$$
$$\overline{M_2} = -1 \tag{3}$$

δ_{11} and δ_{22} are obtained from the bending moments:

$$\delta_{11} = \int \frac{\overline{M_1}^2}{EI} ds = 2\int_0^{\theta_0} \frac{r^2(\cos\theta - \frac{\sin\theta_0}{\theta_0})^2}{EI} \cdot r d\theta = \frac{2r^3}{EI}\left(\frac{\theta_0}{2} - \frac{\sin^2\theta_0}{\theta_0} + \frac{1}{4}\sin 2\theta_0\right)$$
$$\delta_{22} = \int \frac{\overline{M_2}^2}{EI} ds = 2\int_0^{\theta_0} \frac{r d\theta}{EI} = \frac{2r\theta_0}{EI} \tag{4}$$

(4) Solve for the free terms Δ_{1P} and Δ_{2P}. The bending moment of the basic structure under load $F/2$ is

$$M_P = \frac{Fr\sin\theta}{2} \tag{5}$$

Substitute the bending moment into the following equation to find the free terms Δ_{1P} and Δ_{2P}:

$$\Delta_{1P} = \int \frac{\overline{M_1} M_P}{EI} ds = -\frac{Fr^3}{EI}\left(\frac{\cos 2\theta_0}{4} + \frac{\sin\theta_0}{\theta_0} - \frac{\sin\theta_0\cos\theta_0}{\theta_0} - \frac{1}{4}\right)$$
$$\Delta_{2P} = \int \frac{\overline{M_2} M_P}{EI} ds = \frac{Fr^2}{EI}(\cos\theta_0 - 1) \tag{6}$$

(5) Internal force calculation

The redundant unknown forces X_1 and X_2 are

$$X_1 = -\frac{\Delta_{1P}}{\delta_{11}} = \frac{F\left[\frac{1}{4}(\cos 2\theta_0 - 1) + \frac{\sin\theta_0}{\theta_0}(1-\cos\theta_0)\right]}{\theta_0 + \frac{1}{2}\sin 2\theta_0 - \frac{2\sin^2\theta_0}{\theta_0}}$$
$$X_2 = -\frac{\Delta_{2P}}{\delta_{22}} = \frac{Fr(1-\cos\theta_0)}{2\theta_0} \tag{7}$$

(6) Solve the bending moment

The bending moment of a single curved beam under load concentrated at the top is obtained from the following equation:

$$M = \overline{M_1}X_1 + \overline{M_2}X_2 + \overline{M_3}X_3 + M_P \tag{8}$$

$$M = Fr\left[\left(\frac{\sin\theta_0}{\theta_0}-\cos\theta\right)\frac{\left[\frac{1}{4}\left(\cos 2\theta_0-1\right)+\frac{\sin\theta_0}{\theta_0}\left(1-\cos\theta_0\right)\right]}{\theta_0+\frac{1}{2}\sin 2\theta_0-\frac{2\sin^2\theta_0}{\theta_0}}+\frac{1-\cos\theta_0}{2\theta_0}-\frac{\sin\theta}{2}\right] \tag{9}$$

3.2 Cracking load analysis

The cracking moment of a UHPFRC section $M_{cr}=M_s+M_c=f_tW_s$, which is the sum of the UHPFRC matrix bending moment and the longitudinal tensile reinforcement bending moment (Fig. 14), where M_{cr} is the cracking moment of the UHPFRC-reinforced beam; M_s is the bending moment of the longitudinal reinforcement; M_c is the bending moment of the UHPFRC matrix; W_s is the elastic resisting moment of the beam cross-section considering the effect of plastic deformation in the tensile zone; f_t is the tensile stress of the UHPFRC matrix.

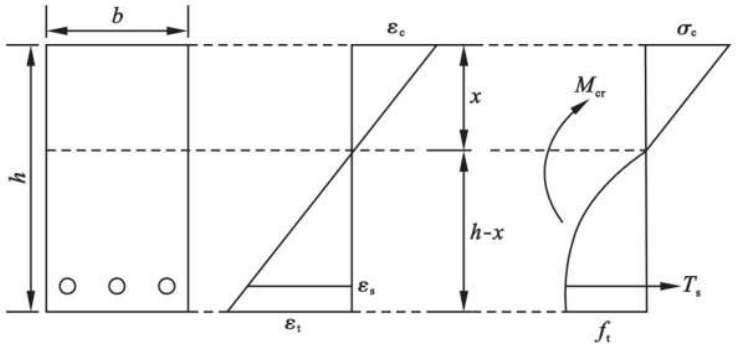

Figure 14 *Cracking moment schematic or reinforced UHPFRC section.*

The concrete stress distribution in the tensile region of the reinforced UHPFRC beam was simplified as triangular and rectangular distribution [19]. The concrete compressive stress in the compression region was small, and the stress distribution was approximately triangular, as shown in Fig. 15. According to the above test results, the concrete tensile strain value was 468 με, which is converted to 0.76 f_t, where ft represents the peak stress of the axial tension of the UHPFRC. E_c is the elastic modulus of concrete; E_s is the elastic modulus of steel; ε_c is the concrete compressive strain at the edge of the compression zone under the cracking load; ε_{t0} is the initial cracking strain of the UHPFRC. F_c is the combined force on the concrete in the compression zone. F_{t1} is the combined force on the concrete with triangular distribution in the tensile zone. F_{t2} denotes the combined force of the trapezoidal distribution in the concrete in the tensile zone. F_{t1} is the combined force on the concrete with a triangular distribution in the tensile zone. F_{t2} denotes the combined force on the concrete with trapezoidal distribution in the tensile zone. T_s denotes the combined force on the longitudinal tensile reinforcement in the reinforced beam; x_0 denotes the height of the compression zone of the UHPFRC; X_t denotes the height of the tensile zone of the UHPFRC. f_t denotes the axial tensile peak stress in the UHPFRC. The calculated cracking moment of the UHPFRC-reinforced beams is shown in Eq. (10).

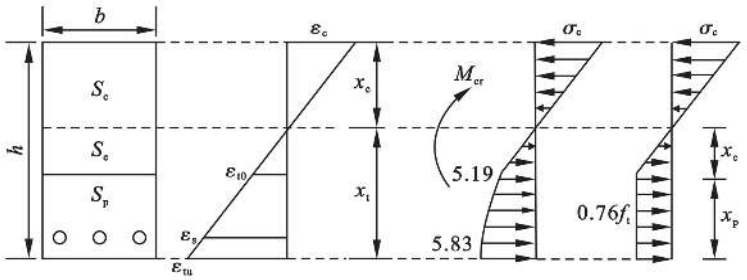

Figure 15 *Distribution of cracking moment stresses in UHPFRC beams.*

$$M_{cr}=1.7b\frac{x_c^{\ 2}}{h-x_c}\varepsilon_{t0}E_cx_c/3+2.45bf_t(h-x_c)^2+1.7E_sA_s\frac{(h_0-x_c)^2}{h-x_c}\varepsilon_{t0} \tag{10}$$

The mid-span section the curved beam cracked, *i.e.*, ϑ=0. The coupling Equation (9) describes the crack load as follows:

$$F_{cr}=\frac{M_{cr}}{r\left[\left(\frac{\sin\theta_0}{\theta_0}-1\right)\frac{\left[\frac{1}{4}\left(\cos 2\theta_0-1\right)+\frac{\sin\theta_0}{\theta_0}\left(1-\cos\theta_0\right)\right]}{\theta_0+\frac{1}{2}\sin 2\theta_0-\frac{2\sin^2\theta_0}{\theta_0}}+\frac{1-\cos\theta_0}{2\theta_0}\right]} \tag{11}$$

The calculated crack load Fcr was 228 kN/m, the error was 3.6% compared with the experimentally measured value (220 kN/m). The calculated cracking moment after considering the tensile strength of the UHPFRC was in = agreement with the experimentally measured value, which indicates that Equation (11) can be used in applications to calculate the crack load of UHPFRC pipeline by considering the tensile strength of UHPFRC.

3.3 Ultimate load-bearing capacity analysis

Moore [20] considered the existence of four types of plastic hinge damage at hazard points such as the top and bottom of the pipe and the line of origin under trilateral loading conditions. Assuming that plastic hinge damage occurs at the top of the curved beam, the structure rotates at the plastic hinge points under external loading, as shown in Fig. 16.

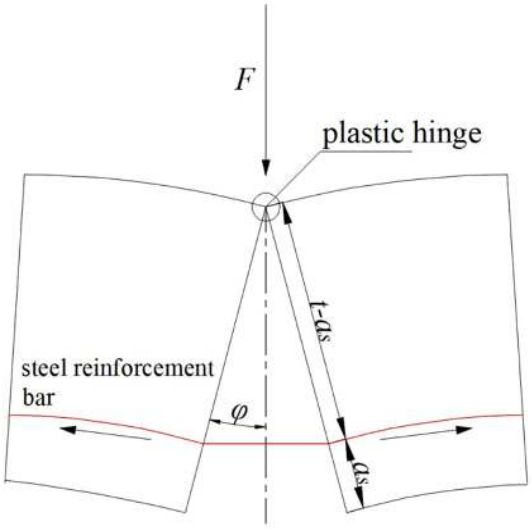

Figure 16 *Deformation model of the top of a curved beam.*

When plastic hinge damage occurred in the structure, the structure did not break into two sections due to the tensile action of the reinforcement. As such, reinforcement yield was the type of damage that occurred in the pipe cross-section based on the elongation of the reinforcement, which is calculated as follows:

$$e_c=2(t-a_s)\varphi \tag{12}$$

where e_c is the elongation of the bar at the top of the curved beam;

t is the wall thickness of the curved beam;

a_s is the thickness of the protective layer;

φ is the rotation angle, which is the ratio of maximum vertical displacement to diameter.

The reinforcement strain is calculated as

$$\varepsilon_c=\frac{e_c}{\theta_0\left(r+a_s\right)}=\frac{2\left(t-a_s\right)}{\theta_0\left(r+a_s\right)} \tag{13}$$

where r is the radius of the inner wall of the curved beam;

ϑ_0 is the angle of the center of the circle corresponding to a semicurved beam.

The reinforcement is in the elastic deformation phase when the strain is small:

$$\sigma_c = E_s \varepsilon_c = \frac{2E_s\left(t-a_s\right)}{\theta_0\left(r+a_s\right)} \tag{14}$$

where Es is the modulus of elasticity of the reinforcement in MPa.

The bending moment is considered for the plastic hinge point to obtain the value of the bending moment at the top pipe section Mc:

$$M_c = \sigma_c A_s\left(t-a_s\right) = \frac{2E_s \varphi A_s\left(t-a_s\right)^2}{\theta_0\left(r+a_s\right)} \tag{15}$$

where As is the cross-section area of the reinforcement.

The hazardous section of the curved beam is the midspan section, i.e., ϑ=0. It is assumed that the curved beam reaches its ultimate capacity Fu when the reinforcement yields, and coupling Equation (9) is derived:

$$F_u = \frac{M_c}{r\left[\left(\frac{\sin\theta_0}{\theta_0}-1\right)\frac{\left[\frac{1}{4}\left(\cos 2\theta_0-1\right)+\frac{\sin\theta_0}{\theta_0}\left(1-\cos\theta_0\right)\right]}{\theta_0+\frac{1}{2}\sin 2\theta_0-\frac{2\sin^2\theta_0}{\theta_0}}+\frac{1-\cos\theta_0}{2\theta_0}\right]} \tag{16}$$

Input the actual data to obtain the ultimate load calculation value Fu of the pipe, 458.05 kN/m, which is similar to the value measured in the three-edge bearing test. The error is 4.8%, and the difference between the theoretical value and the test value is small, indicating that the UHPFRC pipe bearing capacity model can be used as a theoretical calculation model.

4 NUMERICAL SIMULATION ANALYSIS OF PIPELINE PERFORMANCE

4.1. Modeling

Based on the above experimental data, a concrete damaged plasticity model of UHPFRC pipeline is established based on ABAQUS and compared with the above experimental results to verify the reasonableness of the analysis method and provide a reference for the nonlinear finite element analysis of UHPFRC.

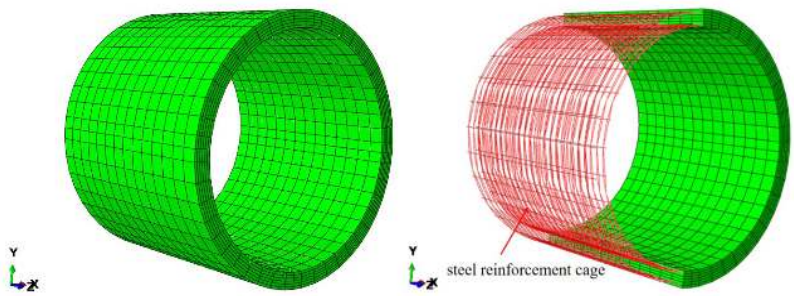

Figure 17 *Finite element numerical modeling of three-edge bearing test.*

The numerical finite element model used for simulating the three-edge bearing test of the pipe is depicted in Figure 17. This model primarily comprises two integral components, the concrete pipe and reinforcing cage, with both dimensions and

reinforcement ratios aligned with the prior experimental specifications. It is established that the concrete pipe should be modeled using an eight-node, uncoordinated, hexahedral solid elements (C3D8I) following an analysis of various elements configurations and mesh densities. This element was chosen for its balance of high precision and reduced computational expense. The reinforcing cage was modeled using a two-node, three-dimensional truss elements (T3D2), with the details of the elements types and quantities outlined in Table 1. Additionally, an embedded region interaction was implemented to simulate the interactive forces between the steel reinforcement and concrete pipe. Notably, a simply supported configuration was adopted for the reinforced concrete pipe in the test, necessitating the application of a translational constraint at the base of the lower loading beam. Furthermore, a reference point was coupled to the upper surface of the upper loading beam, facilitating the control of the magnitude of the displacement loading and the monitoring of the resultant concentrated force within the pipe.

Table 1 Type and number of three-edge bearing test model units for test pipe.

Model Part	Number of units	Unit Type
Concrete pipe	4200	C3D8I
Reinforcement cage	4860	T3D2

4.2. constitutive model

(1) Constitutive model of UHPFRC uniaxial compression

The principal relationship of UHPFRC compression was adopted from the model of Yang Jian [21].

$$\sigma(\varepsilon)=\begin{cases} f_c\dfrac{n\xi-\zeta^2}{1+(n-2)\xi} & (0<\varepsilon<\varepsilon_0) \\ f_c\dfrac{\xi}{2(\xi-1)^2+\xi} & (\varepsilon\geq\varepsilon_0) \end{cases} \tag{17}$$

where $\varepsilon_0=3500\mu\varepsilon$, $\xi=\varepsilon/\varepsilon_0$, fc is the compressive strength, and $n=E_c/E_s$ is the ratio of the initial modulus of elasticity to the cut line modulus at the peak point. Calculations were conducted based on the values obtained from the test of the material properties.

(2) Uniaxial tensile constitutive model of UHPFRC

The tensile elasticity and strain hardening phases of UHPFRC were modeled using the bifold strengthening model proposed by Zhe Zhang et al. [22].

$$\sigma(\varepsilon)=\begin{cases} \dfrac{f_{ct}}{\varepsilon_{ca}}\varepsilon & (0<\varepsilon<\varepsilon_{ca}) \\ f_{ct} & (\varepsilon_{ca}<\varepsilon<\varepsilon_{pc}) \end{cases} \tag{18}$$

where f_{ct} is the average tensile strength, averaged according to the initial cracking strength and ultimate strength of the UHPFRC; ε_{ca} and ε_{pc} are the peak and ultimate tensile strain of the elastic phase, respectively, the values of which were obtained from the measured material properties.

(3)Other plasticity parameters

The plasticity parameters of the concrete need to be selected in addition to the intrinsic parameters. The values of specific parameters were obtained from pipe manufacturers and are shown in Table 2.

Table 2 Values of other plasticity parameters.

α/°	E_c/MPa	Poisson's ratio for concrete	Eccentricity	f_{b0}/f_{c0}	k_c	μ	E_s/MPa	Poisson's ratio for steel reinforcement
38°	45300	0.2	0.1	1.16	0.667	0.0001	195000	0.3

Note: α = expansion angle; E_c = modulus of elasticity of concrete; f_{b0}/f_{c0} = ratio of compressive to tensile strength of concrete in both directions; k_c = ratio of second stress-invariant tensile meridian and compressive meridian at initial yielding; μ = viscous parameter; E_s = modulus of elasticity of the reinforcement.

4.3. Load–Displacement Curve

A comparison of the load–displacement curves for this three-edge bearing test pipe, the numerical simulation of the test pipe, and the numerical simulation of the C50 grade concrete pipe is shown in Figure 18.

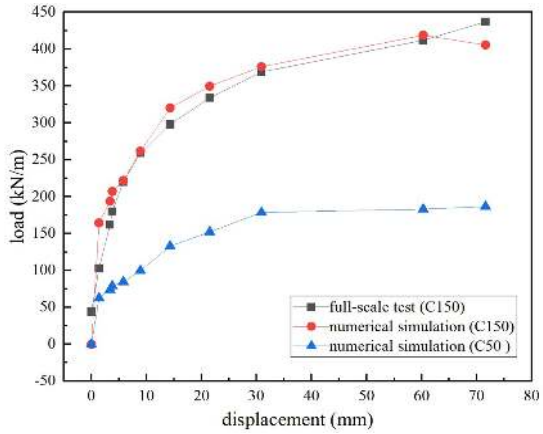

Figure 18 *Load–displacement curves for numerical simulation and three-edge bearing test.*

The numerical simulation results were consistent with the test results in terms of the displacement–load curve pattern before the peak load was reached, and the model was able to reflect the load-bearing and deformation performance of this ultra-high performance concrete jacking pipe. In addition, the bearing capacity and deformation ability of the UHPFRC pipe were notably higher than those of C50-grade concrete pipe. The peak load of UHPFRC pipe was 2.55 times higher than that of ordinary concrete pipe when they were the same size.

4.4. Crack development

Reference is made to the method proposed by Nogales et al. [23] to characterize the total crack width using the relative displacement of the two nodes in the plastic zone in ABAQUS; the results are shown in Fig. 19. The crack width during the concrete cracking stage was characterized by measuring the change in the relative distance between point 1 and point 2 in the plastic damage region at the top of the model pipe. After concrete cracking, this crack monitoring method was found to be reasonable considering the dense grid division and the small spacing between points on both sides where plastic cracking occurred, although the crack width obtained included some of the elastic deformation of the concrete.

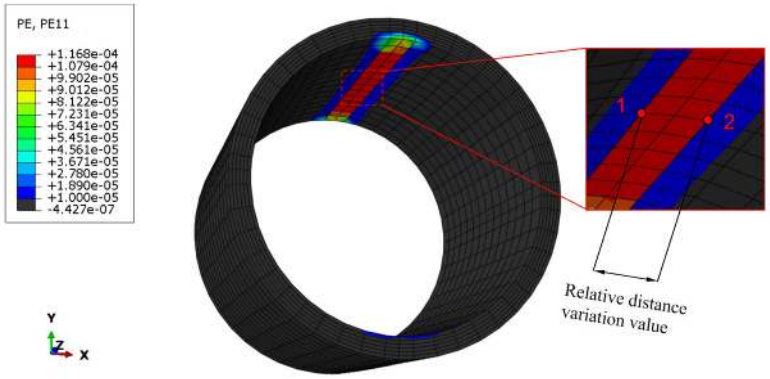

Figure 19 *Measurement schematic of numerical simulation of crack width.*

The numerical simulation statistics of the crack width evolution at the top of the pipe with loading were compared with the results of the three-edge bearing test, with the results shown in Fig. 20. In the early stage, the numerical simulation results reflected the crack development pattern, which was consistent with the results of the three-edge bearing test. The acceleration of crack width increased with increasing load. The load was 220 kN/m when the crack at the top of the pipe was 0.2 mm wide in the three-edge bearing test; the crack load according to the numerical simulation results was 237.13 kN/m, yielding an error of 7.79%. The numerical simulation results were slightly smaller than the test

results in the preloading period because the method could not fully simulate the concrete disconnection. Overall, the simulation and statistical method accurately predicted the precracking load of fiber-reinforced concrete pipe.

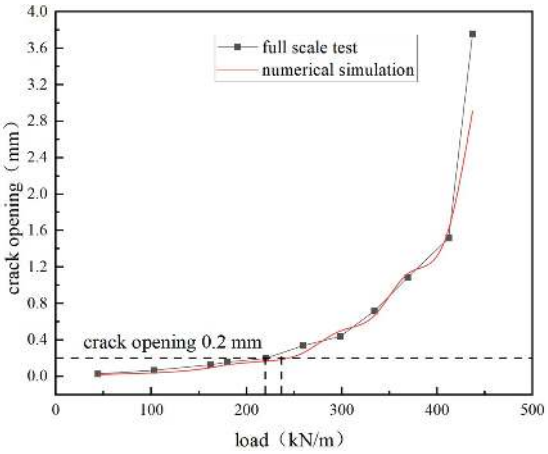

Figure 20 *Comparison of numerical and experimental curves of load–crack width evolution of test pipes.*

In response to the numerical simulation results and the crack extension results obtained from the test results, the load and crack fitting equation for this test pipe was fitted using the origin software as $w = 0.0263e^{0.424q}$.where w is the crack opening; q is the load.

4.5. Pipeline Damage Patterns

The critical cross-section of the pipe in the loading process is analysed by the stress distribution cloud, the stress contour plot of the pipe when the vertical displacement at the pipe's apex reaches 6.5 mm in the simulation is presented in Figure 21, where S11 indicates the horizontal stress (X direction), and S22 indicates the vertical stress (Y direction). The plot reveals that the outer wall of the pipeline's concrete experienced compressive stress at the top and bottom during loading, whereas the inner wall experienced tension. The inner-wall concrete at the top attained its ultimate tensile strength of 6.4 MPa upon application of a concentrated load of 213 kN/m. The concrete on both sides of the pipe experienced tensile stress on the outer wall and compressive stress on the inner wall, with a maximum tensile stress of 2.49 MPa, which was still within the elastic range. This suggests that the top concrete reaches the plastic tensile damage stage prior to the concrete on the sides. The outer-wall concrete on both sides of the pipe attained its peak tensile strength and transitioned into the plastic phase as the vertical displacement at the pipe's apex increased to approximately 8.5 mm. At this juncture, the maximum von Mises stress of the pipeline's concrete, depicted in Figure 22, was 8.94 MPa, which is substantially lower than the concrete's compressive strength. This indicates that, during the three-edge bearing test, tensile cracks initially form in the tensile zone of the pipeline.

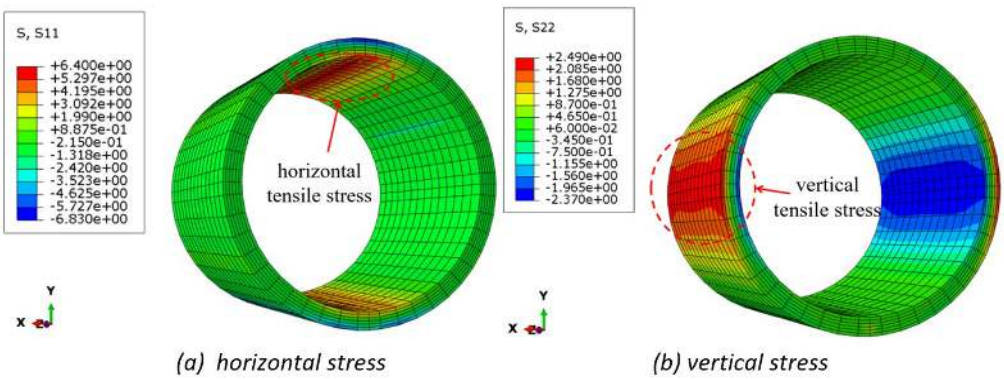

Figure 21 *Stress cloud at the top of the pipe when the concrete reaches its tensile strength.*

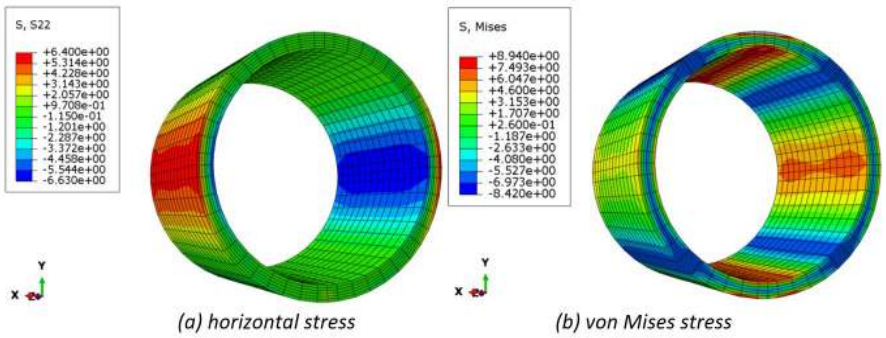

Figure 22 *Stress cloud of pipe-waist concrete when it reaches tensile strength.*

The strain and vertical displacement of the inner ring reinforcement when the pipe is damaged are shown in Fig. 23: 540 MPa (i.e., the ultimate tensile strength) when loaded to 418.74 kN/m and 61.2 mm, respectively. Therefore, the ultimate load of the pipe was calculated to be 418.74 kN/m using the finite element model, yielding a 4.2% error compared with that of the ultimate load (437 kN/m) obtained from the three-edge bearing test. The error was 4.2% compared with the ultimate load (437 kN/m) obtained from the three-edge bearing test. The results indicate the reliability of the finite element model.

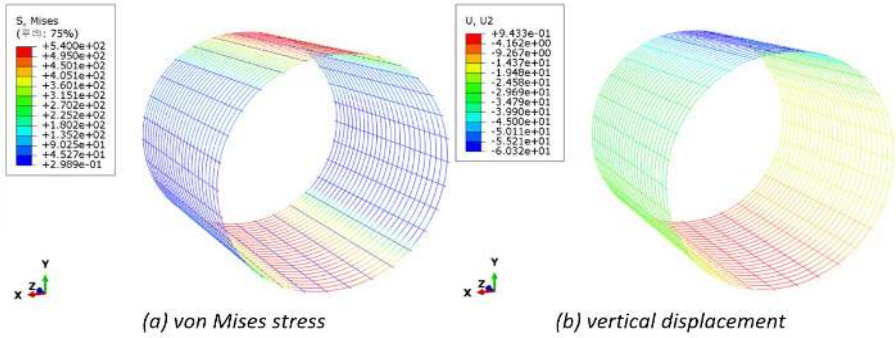

Figure 23 *Stress cloud of inner ring reinforcement at ultimate tensile strength.*

Figure 24 shows the damage the pipeline at the end of loading in the simulation with the distribution of plasticity zones, from which it can be seen that there is a large plasticity of the concrete in the top compression zone of the pipeline at the time of damage, indicating that after the damage of the concrete in the tensile zone, the circumferential reinforcement in the tensile zone reaches the ultimate strain, and the test pipeline reaches the maximum load bearing capacity, which exhibits the characteristics of gradual bending damage. At this time, comparing the plastic deformation area of the compression zone at the top and bottom of the pipe, the plastic deformation area of the concrete in the tensile zone on the left and right sides of the pipe is larger in scope but smaller in deformation, which is the same as the result that the crack width at the top and bottom of the pipe in the three-edge bearing test is larger than that of the left and right sides but the distribution range is smaller than that of the left and right sides, and the plastic deformation area in the simulation result is the same as that in the distribution of cracks in the three-edge bearing test in Fig.9, so this finite element model can reasonably calculate the damage characteristics of UHPFRC pipe.

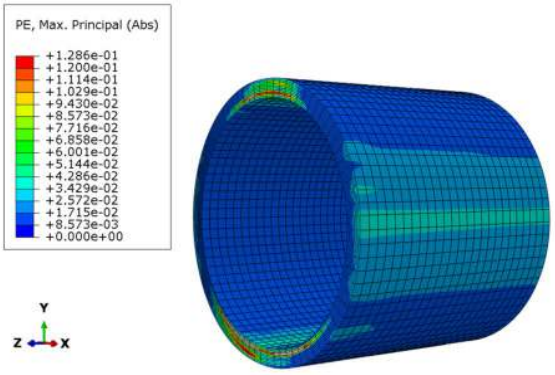

Figure 24 *Damage patterns obtained from pipeline simulation.*

5 OTHER POSSIBLE FORMS OF DAMAGE

Due to the design of the pipe, in the trilateral loading test, the UHPFRC has not yet reached the compressive strength when loaded to the pipe damage, the inner ring tensile reinforcement yielded, and then the concrete compression zone was compressed, which was characterised by the damage of fewer reinforcements. In the case of reasonable reinforcement, the damage of UHPFRC pipe under three-sided loading test conditions should be manifested as the yielding of tensile reinforcement in the inner ring and the destruction of concrete in the top compression zone at the same time. If the reinforcement ratio of the inner and outer ring circumferential reinforcement does not match, the damage of the pipe may be manifested as yielding of the left and right side tensile reinforcement. Subsequent studies can be conducted to investigate the different damage modes of UHPFRC pipes considering the tensile strength of UHPFRC.

6 CONCLUSIONS

Bearing performance test were carried out, a bearing capacity calculation model was established, and numerical simulation analyses were carried out on test pipe with the following parameters: inner diameter of 2.5 m, wall thickness of 180 mm, double-layer reinforcement, 10 spaced at 120 mm on the outside, 10 spaced at 100 mm on the inside, a protective layer thickness of 30 mm on the outside, protective layer thickness of 25 mm on the inside, C150 ultra-high-performance concrete for the pipe, and HRB400-grade reinforcement. The mechanical properties of this pipe were systematically studied, and the following results were obtained:

(1) The test-measured maximum displacements of the pipe in the horizontal and vertical directions were 64.3 and 71.6 mm, respectively; the crack load was 232 kN/m; and the destructive load was 437 kN/m .

(2) The deformation and damage laws of the UHPFRC jacked pipe under radial loading were determined. The damage pattern, deformation, and internal reinforcement strain of the UHPFRC pipe under radial loading conditions were obtained. Four main cracks and several secondary cracks appeared during the loading process, and the concrete finally spalled, the top tensile reinforcement yielded, and the concrete in the compression zone was not crushed. The damage pattern showed that the top tensile reinforcement bar had yielded.

(3) The pipe is simplified as a curved beam for analysis, and the bearing capacity calculation model of UHPFRC pipe is established, considered the tensile strength of the UHPFRC in the tensile zone of the pipeline as well as the damage mode, and derived the cracking moment of the UHPFRC beams. Comparison of the simulated and calculated values of the ultimate loads for the case of under-reinforced damage showed consistent results, which indicates the reliability of the proposed computational model. The design of UHPFRC pipelines should consider the tensile strength of the UHPFRC in the tensile zone.

(4) The load–displacement curves in the pipe finite element model under radial loading conditions were calculated using ABAQUS to obtain the cracking damage pattern of the pipe. The results were verified with the experimental data, which demonstrates that the model developed in this study can be applied to the finite element analysis of UHPFRC pipeline. The macroscopic damage process and the load-bearing performance of the UHPFRC pipeline can be accurately predicted through the finite element numerical simulation method. The peak radial loading capacity of UHPFRC pipe was 2.55 times higher than that of C50 grade concrete pipe of the same size.

Acknowledgements

This research is supported by the technology program of State Grid Co., Ltd. of China (No.5200-202322138A-1-1-ZN)

Author's Contribuitions: Conceptualization, Lei He and Li Zhou; Methodology, Lei He; Investigation, Shanqing Ma, Wei Wang and Yuan Lu; Writing - original draft,Lei He, Shanqing Ma; Writing - review & editing, Shanqing Ma; Funding acquisition, Li Zhou; Resources, Zengli Shi and Yuan Lu; Supervision, Wei Wang.

Editor: Marco L. Bittencourt

References

1. X. L. Cheng, R. Mu, X. Y. Liu, Research progress on the preparation and mechanical properties of ultra-high performance concrete [J/OL]. Bulletin of the Chinese Ceramic Society, 1-21, 2024.

2. M. Chen, J. Feng, T. Zhang, Study on dynamic splitting tensile properties of ultra-high performance concrete after high temperature [J/OL]. Journal of Building Materials, 1-12.

3. B. He, H. E. Zhang, M. R. Zhao, et al, Tensile behavior and acoustic emission damage temporal evolution of UHPFRC under ultra-low temperature-high temperature alternating environment [J]. Journal of Building Structures,2024,45(09):1-12. DOI:10.14006/j.jzjgxb.2023.0529.

4. J. C. Han, L. M. Lü, L. Hu, et al, Dynamic Failure Mechanism and Mechanical Property Enhancement of Steel Fiber Ultra - High Performance Concrete. Protective Engineering, 46(06), 9-17.

5. J. Y. Zhang, A Review of the Research on the Influence of Steel Fibers on the Mechanical Properties of Ultra - High Performance Concrete. Sichuan Building Materials, 50(08), 17-18+21.

6. D. G. Feng, Research on the Shear Resistance of Ultra - High Performance Fiber Reinforced Concrete Strengthened RC Beams. Western China Communication Science & Technology, (01), 126-128. DOI:10.13282/j.cnki.wccst.2024.01.037.

7. T. Zhang, Application of jacked pipe construction technology under urban traffic main roads [J]. Stone Industry,2024,(08):132-134.DOI:10.14030/j.cnki.scaa.2024.0385.

8. J. F. Li, Research on early shrinkage deformation and crack development law of ultra-high performance concrete [D]. Northeast Electric Power University, 2023.DOI:10.27008/d.cnki.gdbdc.2023.000201.

9. M. Jian, Research on composition design and bonding performance of basalt fiber reinforced ultra-high performance concrete [D]. Yangzhou University, 2023.DOI:10.27441/d.cnki.gyzdu.2023.002476.

10. X. Y. Yan, C. Yu, S. H. Zhai, Experimental study on mechanical properties of joints of segmented prefabricated pipe gallery segments [J]. Sichuan Building Science Research,2017,43(06):28-31.

11. L. B. Liu, Performance and structural analysis of ultra-high performance concrete composite pipe [D]. Wuhan University of Technology,2018.

12. Y. Yang, R. Chen, Q. W. Huang, B. C. Chen, W. Huang, J. G. Wei, Optimization design and life-cycle cost analysis of UHPFRC pipe gallery [J]. Journal of Ningxia University (Natural Science Edition),2018,39(03):227-233.

13. T. Haktanir, K.Ari, F. Altun, et al, A comparative experimental investigation of concrete, reinforced-concrete and steel-fibre concrete pipes under three-edge-bearing test[J]. Construction & Building Materials, 2007, 21(8): 1702-1708.

14. C. Macdonald, J. Trangsrud.Steel fiber product introduction through pre-cast reinforced concrete pipe[J]. ACI Special Publication, 2004, (222): 185-99.

15. Y. Park, A. Abolmaali, M. Mohammadagha, et al, Structural performance of dry-cast rubberized concrete pipes with steel and synthetic fibers[J]. Construction & Building Materials, 2015, 77:218-226.

16. Y. Xu, P. Zhang, C. Zeng, et al, Research on Calculation Model of Frictional Resistance around Rectangular Pipe Jacking Based on Effective Earth Pressure [J/OL]. Chinese Journal of Geotechnical Engineering, 1-11 [2024-12-17]. http://kns.cnki.net/kcms/detail/32.1124.TU.20241105.1713.002.html.

17. Y. Zhou, H. Zhou, M. Yuan, et al, Calculation Method of Jacking Force for Circular Curve Pipe Jacking Considering Pipe-Soil Contact State [J]. Bulletin of Geological Science and Technology, 2023, 42(03): 63-71. DOI: 10.19509/j.cnki.dzkq.tb20210729.

18. M. Z. Gong, A. X. Pan, Z. L. Zhang, et al, Research on the Pull - out Behavior of Steel Fibers in Ultra - High Performance Fiber - Reinforced Concrete. Bulletin of the Chinese Ceramic Society, 42(08), 2764-2772. DOI:10.16552/j.cnki.issn1001-1625.2023.08.008.

19. X. Lu, Calculation method of active powder concrete rectangular cross-section reinforced beams subjected to bending in positive section [D]. Beijing: Beijing Jiaotong University, 2011.

20. I. D. Moore, N. A. Hoult, K. MacDougall, Establishment of appropriate guidelines for use of the direct and indirect design methods for reinforced concrete pipe[J]. AASHTO Standing Committee on Highways, 2014.

21. J. Yang, Study on the stress performance of ultra-high performance concrete beams with CFRP prestressing tendons [D]. Hunan University, 2007.

22. Z. Zhang, et al, Test on axial tensile performance of ultra-high performance concrete [D]. China Highway Journal, 2015, (8): 50-58.

23. A. Nogales, A. De La Fuente, Crack width design approach for fibre reinforced concrete tunnel segments for TBM thrust loads[J]. Tunnelling and Underground Space Technology, 2020,98: 17.